Submarine Permafrost Map in the Arctic Modeled Using 1-D Transient Heat Flux (SuPerMAP)

P. P. Overduin[1] , T. Schneider von Deimling[1], F. Miesner[1] , M. N. Grigoriev[2] , C. Ruppel[3] , A. Vasiliev[4] , H. Lantuit[1] , B. Juhls[5] , and S. Westermann[6]

[1]Alfred Wegener Institute, Helmholtz Centre for Polar and Marine Research (AWI), Potsdam, Germany, [2]Melnikov Permafrost Institute, Siberian Branch, Russian Academy of Sciences, Yakutsk, Russia, [3]U.S. Geological Survey, Woods Hole, MA, USA, [4]Earth Cryosphere Institute of Tyumen Scientific Center, Siberian Branch, Russian Academy of Sciences and Tyumen State University, Tyumen, Russia, [5]Institute for Space Sciences, Freie Universität Berlin, Berlin, Germany, [6]Geoscience Department, University of Oslo, Oslo, Norway

Abstract Offshore permafrost plays a role in the global climate system, but observations of permafrost thickness, state, and composition are limited to specific regions. The current global permafrost map shows potential offshore permafrost distribution based on bathymetry and global sea level rise. As a first-order estimate, we employ a heat transfer model to calculate the subsurface temperature field. Our model uses dynamic upper boundary conditions that synthesize Earth System Model air temperature, ice mass distribution and thickness, and global sea level reconstruction and applies globally distributed geothermal heat flux as a lower boundary condition. Sea level reconstruction accounts for differences between marine and terrestrial sedimentation history. Sediment composition and pore water salinity are integrated in the model. Model runs for 450 ka for cross-shelf transects were used to initialize the model for circumarctic modeling for the past 50 ka. Preindustrial submarine permafrost (i.e., cryotic sediment), modeled at 12.5-km spatial resolution, lies beneath almost $2.5 \times 10^6 \text{km}^2$ of the Arctic shelf. Our simple modeling approach results in estimates of distribution of cryotic sediment that are similar to the current global map and recent seismically delineated permafrost distributions for the Beaufort and Kara seas, suggesting that sea level is a first-order determinant for submarine permafrost distribution. Ice content and sediment thermal conductivity are also important for determining rates of permafrost thickness change. The model provides a consistent circumarctic approach to map submarine permafrost and to estimate the dynamics of permafrost in the past.

1. Introduction

Permafrost is defined as Earth material with a perennially cryotic (< 0° C) temperature (van Everdingen, 1998). Submarine (or subsea or offshore) permafrost is permafrost overlain by a marine water column. Most submarine permafrost occurs in the Arctic (Brown et al., 2001), is relict terrestrial permafrost (Kitover et al., 2015; Romanovskii et al., 2004), and has been degrading since being inundated during sea level rise after the Last Glacial Maximum (Osterkamp, 2001). Submarine permafrost may or may not contain ice (i.e., be partially frozen), depending on its temperature, salt content, sediment grain size, and composition. While important to coastal and offshore processes and infrastructure (Are, 2003), recent attention has focused on its role in the global carbon cycle. Large amounts of fossil organic carbon (McGuire et al., 2009) and greenhouse gases (Shakhova & Semiletov, 2007) may exist intrapermafrost and/or subpermafrost. Ruppel (2015) estimates that 20 Gt C (2.7×10^{13} kg CH_4) may be sequestered in gas hydrates associated with permafrost, mostly in Arctic Alaska and the West Siberian Basin. Methane in particular may be present in large amounts in gas hydrate form (e.g., Dallimore & Collett, 1995) and be destabilized by permafrost thaw (e.g., Frederick & Buffett, 2015), although methane emissions may be oxidized before reaching the atmosphere (Overduin et al., 2015; Ruppel & Kessler, 2017) or better explained by geological sources (Anisimov et al., 2014). Given projected future decreases in sea ice cover, thickness, and duration on the Arctic shelves, water temperatures are expected to rise at an increasing rate, increasing heat transfer to shelf sediments and accelerating submarine permafrost thaw. The release of stabilized, contained, or trapped greenhouse gases from submarine permafrost is thus a potential positive feedback to future climate warming.

Most submarine permafrost is relict permafrost that has developed where glaciation, climate, and relative sea level fluctuation permit terrestrial permafrost to be transgressed by rising sea level. Large warm-based

glacial ice masses during cold climate periods prevented permafrost from forming. We thus expect submarine permafrost on the continental shelf regions that were not glaciated: most of the shelves of the marginal seas of Siberia (Kara, Laptev, East Siberian, and Chuckhi) and the Chukchi and Beaufort Sea of North America. The International Permafrost Association (IPA) permafrost map (Brown et al., 2001) shows submarine permafrost based on global sea level reconstructions, modern bathymetry, and the assumption that permafrost persists out to about the 100-m isobath. Existing maps focus on the regional scale (Nicolsky et al., 2012; Romanovskii et al., 2004; Vigdorchik, 1980a, 1980b; Zhigarev, 1997) and are based on different combinations of theoretical and empirical approaches to simulate permafrost evolution over time. Some of these tend to reproduce coverage similar to the IPA map, with some combination of cryotic and ice-bonded permafrost, for example, for the Laptev Sea (Nicolsky et al., 2012; Romanovskii et al., 2004; Tipenko et al., 1999), whereas other models produce a more conservative estimate of isolated regions of near-shore ice-bonded permafrost (Zhigarev, 1997).

Nicolsky et al. (2012) and Lachenbruch (1957, 2002) demonstrate that thermokarst lakes, rivers, and saline sediments can form ice-poor regions within millennia after transgression. Nonetheless, the Last Glacial period and continental climate of eastern Siberia led to particularly cold and deep permafrost over a broad expanse of continental shelf, permafrost that persists until today. Publicly available observational data are limited to shallow boreholes drilled from ships (Kassens et al., 1999; Rekant et al., 2015) or from the sea ice (Blasco et al., 2012; Dallimore, 1991; Winterfeld et al., 2011), a few deeper scientific boreholes, geophysical records from industrial boreholes in the Beaufort Sea (e.g., Hu et al., 2013), and geophysical records (e.g., Portnov et al., 2016; Rekant et al., 2015). Data from boreholes deep enough to penetrate permafrost in the prodeltaic region of the Mackenzie River and on the Alaskan Beaufort shelf have been published and analyzed for the depth of the base of permafrost (Brothers et al., 2016; Hu et al., 2013; Issler et al., 2013; Ruppel et al., 2016). Relating geophysical observations to permafrost depth, lithology, cryostratigraphy, or sediment temperature is not trivial. Hu et al. (2013) examine over 250 borehole records, including over 70 offshore boreholes, and find permafrost 100 to 700 m thick north of the Mackenzie Delta and eastward. Ruppel et al. (2016) and Brothers et al. (2016) analyze available borehole and seismic data from the U.S. Beaufort Sea to provide a conservative representation of permafrost extent on the shelf: it is restricted to waters less than 20 m deep and closer than 30 km from shore.

Thus, regional modeling efforts and observational studies differ, suggesting an incomplete understanding of permafrost dynamics on the shelf, and observations suggest significant spatial variability at the regional to circumarctic scale. Given its potential role in storing methane and mitigating its emission, and given that the Arctic shelf seas are undergoing unprecedentedly rapid changes, understanding of this component of the global climate system is important. A globally consistent model of submarine permafrost evolution may explain its distribution and vulnerability to the changes currently underway in the Arctic. Such a first-order model can be tested by evaluating whether its results match available observations of subsea permafrost in terms of presence versus absence, lateral and depth extents, and ice content. An evaluation of the sensitivity of these output parameters to input data sets can provide clues as to which improvements are required for better predictive capacity at specific sites.

The objective of this study is to use available circumarctic data sets to model the thermal dynamics of Arctic shelf sediments at the circumarctic scale over multiple glacial-interglacial cycles using a simple first-order model. We hypothesize that submarine permafrost is widespread wherever a lack of glaciation permitted deep and cold permafrost to form during the Late Pleistocene and that degradation since the Holocene has reduced much of this once deeply frozen permafrost to ice-poor permafrost.

2. Method

2.1. Modeled Domain

We used CryoGrid 2, a 1-D heat diffusion model introduced by Westermann et al. (2013). For the purpose of simulating the thermal state of Arctic shelf regions, we have modified and extended the current model in various aspects that we describe in the following.

We focussed on the Arctic shelf between modern isobaths of 0 and 150 m below sea level (m bsl; the pink region in Figure 1). Modeling was performed on a $7,000 \times 7,000$-km grid of 560×560 equidistant points at 12.5-km spacing in the northern polar EASE Grid 2.0 format (Brodzik et al., 2012, 2014). Elevation or bathymetry was averaged for each 12.5-km grid cell from the International Bathymetric Chart of the Arctic

Figure 1. The modeled domain includes Arctic shelf regions with modern water depths less than 150 m (shaded pink). Black points indicate locations modeled for 450-ka runs (Figure 6). Blue lines show the preliminary classification of the Arctic Ocean following the International Hydrographic Organisation (International Hydrographic Organization, 2002), which has been modified to extend to the pole in order to include the entire shelf region. Sites for model sensitivity are marked as red circles.

Ocean (IBCAOv3.0; Jakobsson et al., 2012). Of the resulting 313,600 grid cell centers, 43,459 (6.79×10^6 km²) lay between 0 and 150 m bsl. Of these, we removed cells in the Baltic, surrounding Iceland, in the southern Bering Strait, in the Ob estuary, in the Lena River channel, and all points south of 65°N, leaving a set of 26,333 grid cells covering an area of 4.11×10^6km². Thermal modeling was performed below the ground surface (corresponding to the sea bed, the land surface, or the subglacial surface) to a depth of 6,000 m. Modeled locations were grouped based on Arctic shelf seas as defined by the preliminary system of the International Hydrographic Organisation, modified to extend to the north pole (International Hydrographic Organization, IHO, 2002, the blue polygons shown in Figure 1).

Conductive heat flow below the Earth surface was modeled based on the continuity equation for internal energy E (J/m³)

$$\frac{\partial E}{\partial t} + \frac{\partial}{\partial z} F_{\text{heat}}. \tag{1}$$

We denote the time with t (s) and the vertical coordinate with z (m). The conductive heat flux is given by

$$F_{\text{heat}} = -k(z, T)\frac{\partial T}{\partial z}, \tag{2}$$

where k denotes the thermal conductivity (W·m^{-1}·K^{-1}). Expanding the time derivative of equation (1) as the partial derivatives of T and introducing the water content θ_w (expressed as volume fraction), we obtain

$$\frac{\partial E}{\partial t} = \frac{\partial E}{\partial T}\frac{\partial T}{\partial t} + \frac{\partial E}{\partial \theta_w}\frac{\partial \theta_w}{\partial T}\frac{\partial T}{\partial t}. \tag{3}$$

This can be further reduced with the volumetric heat capacity $c = \frac{\partial E}{\partial T}$ and the latent heat of freezing and melting of water and ice $L_f = \frac{\partial E}{\partial \theta_w}$ to the one-dimensional heat equation:

$$\left(c(z, T) + L_f \frac{\partial \theta_w}{\partial T} \right) \frac{\partial T}{\partial t} - \frac{\partial}{\partial z} \left(k(z, T)\frac{\partial T}{\partial z} \right) = 0. \tag{4}$$

To simplify, the sensible and latent heat terms can be combined to the effective heat capacity c_{eff}:

$$c_{\text{eff}}(z, T) = c(z, T) + L_f \frac{\partial \theta_w}{\partial T}, \tag{5}$$

($\text{J·m}^{-3}\text{·K}^{-1}$). The modifications and additions that we introduced to the main model from Westermann et al. (2013) are described in the following sections.

2.2. Ice Content and Sediment Type

Sediment thermal properties depend on sediment grain size and porosity, temperature, and the concentration of dissolved solids in the pore water. In our model, the latter depends on whether the depositional environment is terrestrial or marine. In order to be able to solve equation (4), we need to obtain an equation for the effective heat capacity and in particular solve $\frac{\partial \theta_w}{\partial T}$. To determine the freezing temperature of the pore solution and the liquid water content, we calculate the effect of the solutes on the water potential as a function of temperature. Ma et al. (2015) give the generalized Clausius-Clapeyron equation as

$$\left(\frac{1}{\rho_w} - \frac{1}{\rho_i} \right) u = L_f \frac{T - T_f^0}{T_f^0}, \tag{6}$$

where u is pressure (Pa), ρ_w and ρ_i are the densities of liquid water and ice (kg/m³), L_f is the latent heat of fusion for water (J/kg), and T and T_f^0 are the temperature and the freezing temperature of free water (K). This assumes the equilibrium case where $u = u_w = u_i$, with u_w and u_i being the gauge pressures of water and ice. When solutes are present in the pore water, an osmotic pressure or potential term,

$$\Pi = RTC, \tag{7}$$

is introduced (Bittelli et al., 2003; Loch, 1978), where R is the universal gas constant (8.3144 J/K) and C is the solute concentration in the pore solution (mol/m³). Thus, equation (6) changes to

$$\frac{u_w - \Pi}{\rho_w} - \frac{u_i}{\rho_i} = L_f \frac{T - T_f}{T_f}, \tag{8}$$

which describes a depression of the temperature at which freezing begins. The freezing point is

$$T_f = T_f^0 - \frac{R T_f^{0^2}}{L_f} N \tag{9}$$

where N is the normality of the solution in equivalents per liter. N can be related to the salinity of the overlying seawater, S, via

$$N = 0.9141 S (1.707 \times 10^{-2} + 1.205 \times 10^{-5} S + 4.058 \times 10^{-9} S^2) \tag{10}$$

based on Klein and Swift (1977) or to molarity, M, of a salt solution via

$$N = \frac{\text{M}}{f_{\text{eq}}}, \tag{11}$$

where f_{eq} is the numbers of equivalents per mole of solute. From equation (8), ignoring the difference in densities of water and ice, the resulting expression for the soil water pressure becomes

$$u_w(T, \theta_w, n_s) = \frac{L_f}{\rho_w} \left(\frac{T - T_f}{T_f} \right) - \frac{RNT}{\rho_w} \left(\frac{1}{\theta_{\text{sat}}} - \frac{1}{\theta_w} \right) \tag{12}$$

for $T < T_f$, and is relative to solute concentration in the total pore space. We use the van Genuchten-Mualem formulation for soil water potential based on the correspondence between drying and freezing, to obtain the freezing characteristic curve as a function of temperature and solute concentration

$$\theta_w(T, n_s) = \theta_{\text{sat}} \left[1 + \left(-\frac{\alpha}{\rho_w g} u_w(T, \theta_w) \right)^{\text{n}} \right]^{\frac{1-\text{n}}{\text{n}}}, \tag{13}$$

where α and n are sediment-dependent Van Genuchten parameters (Dall'Amico et al., 2011) and g is the gravitational constant. Equation (13) gives the liquid water content for differing sediment types as a function of freezing temperature and salinity. Freezing characteristic curves give the unfrozen water content of the sediment as a function of temperature. A comparison of measured (Hivon & Sego, 1995; Overduin et al., 2008) and modeled unfrozen water content is shown in the supporting information (Figure S1). For measured values, salinity was converted to molality using the TEOS-10 toolbox (Millero et al., 2008) for the valences and atomic weight of dissolved salts in seawater or NaCl.

2.3. Stratigraphy

The thickness of sedimentary deposits and their compaction determine porosity and are thus important for pore space and ice content in permafrost. Global maps of total sediment thickness of the oceans and marginal seas based on geophysical observations are available (e.g., Whittaker et al., 2013). This data set (NGDC) demonstrates one of the challenges of working in the Arctic, namely, the paucity of available data: the map covers everything except for the Arctic Ocean and its shelf seas. Sediment thickness along the coasts varies spatially, with high thicknesses where rivers terminate and where glacial outwash contributed to sedimentation (Jackson & Oakey, 1990). Submerged valleys draining the shelf can have locally high rates of sedimentation (Bauch et al., 2001; Kleiber & Nissen, 2000). On the Arctic shelf, sedimentation associated with deglaciation also contributes to this variability (e.g., Batchelor et al., 2013). This spatial variability implies a temporal variability associated with tectonics, sea level change, and glacial dynamics. Rates of sedimentation are typically higher during deglaciation (Bauch et al., 2001) and vary with distance from the coast (Kuptsov & Lisitzin, 1996).

To simulate the effect of repeated transgression on stratigraphy, sediment properties were initialized based on parameterization for marine and terrestrial sediments. Observed linear sedimentation rates for the Arctic shelf region are highly variable. Long-term mean linear sedimentations rate on the shelf are typically on the order of meters per million years, within the range given by Gross (1977) for both marine and terrestrial sedimentation rates and subglacial sediment dynamics (Boulton, 1996). The range of linear sedimentation rates inferred from surface sediment records across the Laptev Sea shelf range from near zero during the Holocene to over 2.5 cm/ka close to the shelf edge (Bauch et al., 2001). Viscosi-Shirley et al. (2003) report rates based on δ^{14}C and ^{210}Pb dating of sediment cores of between 2 and 70 cm/ka for Laptev Sea and 200 and 700 cm/ka for the Chukchi Sea. In both cases the origin of the sediment is over 60% terrigenous or riverine. Kuptsov and Lisitzin (1996) find sedimentation rates of 11–160 cm/ka for the inner Laptev Sea. We choose transgressive and regressive sedimentation rates of 30 and 10 cm/ka, respectively, for the entire shelf region, for circumarctic modeling. The salinity of pore water in marine sediment was set to 895 mol/m^3 for marine sediment. The resulting freezing characteristic curves are shown in the supporting information (Figure S1).

This treatment of sediment dynamics ignored spatial variation in sedimentation rate across the shelf and along the continental margin. By back-calculating sediment accumulation during transgressive and regressive periods, onlapping marine transgression sediment strata and disconformities were created within the model domain, which affected the amount of ice frozen during sea level low-stand ground cooling. In transgressive environments, terrestrial strata typically terminate with an erosional marine ravinement surface called a transgressive nonconformity (Forbes et al., 2015). Such alternating terrestrial and marine sediment layers are strongly suggested by the few cored and well-described offshore cores on the Arctic shelf, which encounter alternating strata of saline and freshwater permafrost (e.g., Blasco et al., 1990; Ponomarev, 1940, 1960; Rachold et al., 2007). These alternations are not generally visible in offshore permafrost temperature records, which are typically near isothermal (Lachenbruch, 1957) but are often suggested by sediment structure visible in geophysical records (e.g., Batchelor et al., 2013; Ruppel et al., 2016). This representation ignores possible deeper variations in salinity due to groundwater or freezing that have been assumed in other models (e.g., salinity increases to 30% at 10-km depth in Hartikainen & Kouhia, 2010).

Coastal erosion and landward migration of the coast associated with transgressions lead to an increase in the elevation of the base level for the Arctic coastal plains. The sedimentary regime landward of the coast is therefore either low or negative. Although differences between regressive and transgressive sediments are accommodated in CryoGrid 2, the model does not yet account for erosion, which, under subaerial conditions, can include denudation and thermokarst processes prior to transgression.

In addition to alternation between transgressive and regressive sedimentation regimes, sediment compaction is an important influence on sediment porosity and thus partially controls sediment ice content. Porosity usually decreases with depth depending on grain geometry, packing, compaction, and cementation (Lee, 2005) and usually changes at the boundary between unconsolidated and consolidated material. Available models of sediment bulk density or compaction are often empirical and based on global deep-sea databases (Gu et al., 2014; Hamilton, 1976; Kominz et al., 2011). The porosity-depth relationship by Lee (2005) ranges from 0.53 at the seafloor to 0.29 at 1,200 m below the sea floor (bsf), based on five wells from
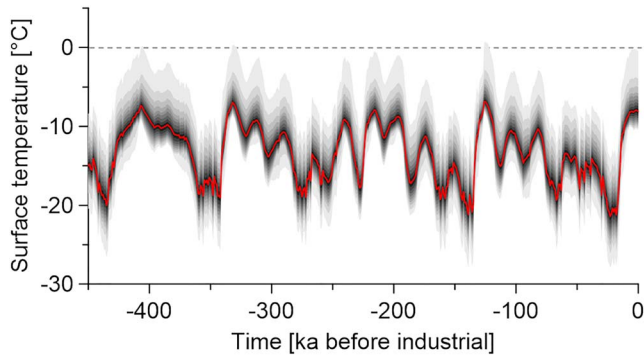
Figure 2. Mean subaerial ground surface temperature forcing data for the past 450 ka from the CLIMBER-2 model (Ganopolski et al., 2010). The gray shaded region around the mean gives the 95% confidence limits in 5% steps for the spatial variability in surface temperature for the set of modeled EASE Grid 2.0 locations.

Milne Point in Prudhoe Bay, Alaska. Gu et al. (2014) combine observations of sediment bulk density for the upper-sediment and lower-sediment compaction from 20,347 samples down to depths of 1,737 m bsf. Extrapolation to depth leads to a porosity of less than 5% at depths greater than 1.2 km. We applied an exponential decrease in porosity from a surface porosity of 0.4 to 0.03 at 1,200 depth, fit to dry bulk density data from Gu et al. (2014) for the shallow Arctic shelf:

$$\eta = 1.80 \, \rho_b^{-1} - 0.6845. \tag{14}$$

A comparison of porosity profiles over depth is presented in the supporting information (Figure S2). The employed parametrization of sediment porosity and pore water salinity must be considered a first-order approximation, which should be refined. The high variability of sediment column thickness found on the shelf; the high proportion of glacially, fluvially, and alluvially deposited terrigenous material; and the presence of transgressive unconformities may lead to shelf sediment columns that differ from from those recorded in marine drilling databases. Our approach represents compaction and the influence of transgressive and regressive cycles but cannot describe the spatial variability of geological structures on the Arctic shelf.

2.4. Boundary Conditions

Permafrost evolution was driven by upper and lower boundary conditions on the modeling domain (0–6,000 m below the surface). This condition was a warming or cooling of the underlying ground via changing surface temperature from above and via geothermal heat flux from below. For the latter, we used the global data set from Davies, (2013, and supporting information Figure S3), based on area-weighted medians of measurements from a global heat flow data set of over 38,000 measurements correlated to geology

$$F_{\text{heat}}(t, 6{,}000\text{m}) = -Q, \tag{15}$$

where Q is the geothermal heat flux (W/m^2). For the former, surface conditions at each modeled time and location were defined as subaerial, submarine, or subglacial depending on modern land surface elevation and bathymetry (Jakobsson et al., 2012), sea level reconstruction (Grant et al., 2014), and glacial ice cover (Ganopolski et al., 2010):

$$T(t, 0\text{m}) = \begin{cases} T_{\text{surface}} & \text{for subaerial} \\ T_{\text{benthic}} & \text{for submarine} \\ T_{\text{basal}} & \text{for subglacial.} \end{cases} \tag{16}$$

In the runs described in this study, we have used spatially explicit surface temperature records simulated by the intermediate complexity Earth System Model CLIMBER-2 (Ganopolski et al., 2010), which also provides glacial ice cover extent and thickness. For this purpose we have interpolated the climate model data (with a resolution of 10° in latitude and 51.4° in longitude) to modeled locations. The mean ground surface temperature and the probability distribution about this median for the modeled domain are shown in Figure 2.

The mean surface temperatures over 450 ka at each modeled location ranged between −17.7 and 0 °C with a mean of −7.3 °C in the modeled domain. An animation of sea level, ice cap distribution, and the modern coastline is available in the supporting information. Deglacial periods and concomitant transgressions are rapid (<10 ka) compared to regressive periods. The area of shelf exposed to subaerial conditions therefore varies over time and space, so that cumulative exposure of the shelf to subaerial conditions increases toward the modern coastline. Given extreme values for mean surfacing temperature forcing (−31.9 and 0 °C), geothermal heat flux (55.7 and 132.6 W/m^2) and sediment stratigraphy (uniformly marine or terrestrial), steady state permafrost thicknesses ranged from 0 to 658 and 1,675 m bsf.
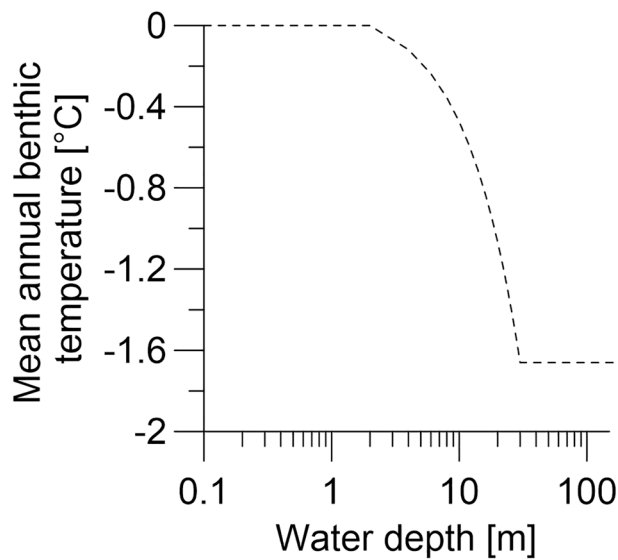
Figure 3. For submarine periods, the upper boundary condition was the benthic water temperature, which was defined as a function of water depth on the Arctic shelf.

There are no regional sea level reconstructions for Arctic shelf seas (Murray-Wallace & Woodroffe, 2014), although many studies provide records of the Holocene transgression (Bauch et al., 2001; Brigham-Grette & Hopkins, 1995). We used the global scale sea level reconstruction from Grant et al. (2014), which covers five glacial cycles based on Red Sea dust and Chinese speleothem records. Inferred ice volumes from any global sea level reconstruction do not necessarily agree with modeled ice volumes provided by CLIMBER-2 output. Our model does not explicitly require ice volume but uses glacial extent to define the upper temperature boundary condition for the modeled permafrost.

By insulating the ground against cold surface air temperatures, thick glacial ice masses influence the temperature regime of subglacial sediments. Ice sheet thicknesses from CLIMBER-2 on a latitude-longitude grid of $0.75° \times 1.5°$ were interpolated to EASE Grid 2.0 resolution, based on the same simulation setup as used for surface air temperatures. We assume a mean annual subglacial temperature of 0 °C, corresponding to warm-based ice masses. Thinner ice sheets can be effective at conducting heat and are more likely to be cold-based, so that CLIMBER-2 ice masses less than 100 m thick were not included. When ice mass distribution extended to regions lying below sea level, we assumed grounding zone and assigned a subglacial temperature.

Once transgressed, cold terrestrial sediments are warmed by the overlying sea water. Forcing temperature at the seabed was set as a function of water depth (Figure 3). In the model, the mean annual benthic temperature was set to 0 °C from the shoreline to 2-m water depth. Between 2 and 30 m, the mean annual benthic temperature decreased linearly from 0 °C to the freezing temperature of sea water. Beyond this depth and to the edge of the shelf a constant benthic temperature was assumed. This results in benthic temperatures as a function of water depth that are comparable to the approach of Nicolsky et al. (2012), based on observational data collected over almost a century from the Siberian shelf region (Dmitrenko et al., 2011). This parameterization does not include the possible thermal coupling of the seabed to the atmosphere in winter through bedfast ice. At water depths less than the maximum thickness of sea ice, bottom-fast sea ice may form, thermally coupling the seabed to the atmosphere and leading to mean annual benthic water temperatures as low as −6 °C in shallow water (Harrison & Osterkamp, 1982; Soloviev et al., 1987). Since this effect is only observed in nearshore shallow water, it probably does not play a role at the temporal and spatial scales modeled here. The influences on benthic temperatures of oceanic currents, stratification, and most importantly riverine and world ocean inflow onto the shelf were not included.

Given the large spatial extent of the circumarctic shelf region and the fact that we have ignored important processes that affect whether a modeled location was subaerial, subglacial, or submarine (e.g., neotectonics and isostasy), the modeled paleo-evolution of permafrost should be regarded as a first-order estimate.

2.5. Modeling

Two model runs were executed, one for selected transects crossing the Arctic shelf from the coast to the 150-m isobath (Figure 1) and a run for the circumpolar Arctic shelf. Transects were modeled for 450 ka using a steady state temperature profile as initial condition, calculated for the sediment profile using the surface temperature and geothermal heat flux as boundary conditions. The circumpolar domain was modeled for 50 ka, initialized with a steady state temperature profile at 50 ka at each modeled location for the first time step. The steady-state solution was calculated based on the temperatures at the lower boundary, $T(t, z) = T(50\text{ka}, 2,000\text{m})$, and the surface, $T(50\text{ ka}, 0\text{ m})$, at the first time step of the model run. Values for the temperatures at 2 km were derived from a correlation of $T(t, 2,000\text{ m})$ with the geothermal heat flux and cumulative surface temperature forcing for 153 locations along 6 transects (Figure 1) from 450 to 50 ka:

$$T(50\text{ka}, 2000\text{m}) = 712.1\, Q + 3.312 \times 10^{-4} \sum_{450\text{ka}}^{50\text{ka}} T_{\text{surf}}(t, 0\text{m}) + 2.076 \tag{17}$$

for which the correlation coefficient was $R^2 = 0.99$ with a standard deviation of the residuals of less than 1.5 °C.
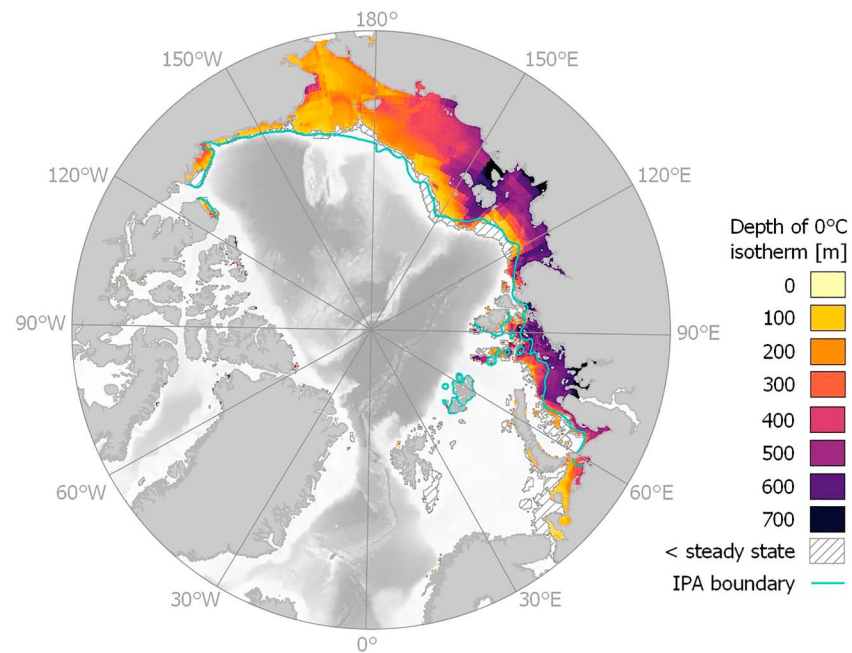
Figure 4. The distribution of modeled postindustrial cryotic sediment and the depth of the lower 0 °C isotherm beneath the Arctic Ocean Shelf seas. Modern Arctic Ocean bathymetry (Jakobsson et al., 2012) and land masses are shown. Submarine permafrost extent from the International Permafrost Association's map is indicated as a cyan line (Brown et al., 2001). In the hatched region, assumed modern sea floor temperatures produce permafrost exceeding modeled depths by more than 50 m.

The CryoGrid 2 model produces the subsurface temperature fields $T_s(t,z)$ for each modeled location from the ground surface or sea bed down to 2 km below the surface. From these data, together with the profile of sediment characteristics, the depth to the lowermost 0 °C isotherm, z_{Pf} (m), the fractional liquid water content $\theta_w(t,z)$, the ice content of the sediment column $\theta_i(t,z)$ (m^3/m^2), and the enthalpy of freezing $H_f(t,z)$ (MJ/m^2) for each subsurface grid cell can be calculated. We define permafrost as cryotic (<0 °C) sediment, regardless of ice content, matching the accepted western definition for terrestrial permafrost (van Everdingen, 1998). Such thermally defined permafrost is not necessarily useful as an indication of past climate or of permafrost response to future climate. Ice content is more important than temperature in terms of the functions of permafrost: providing thermal inertia to perturbation, reducing gas fluxes, and stabilizing gas hydrates; and in terms of observing permafrost using geophysical methods. Seismic methods will only delineate ice-bonded permafrost; permafrost containing little to no ice will not have the elevated propagation velocity needed for seismic refraction or reflection detection. For validation purposes, model output of ice content can match penetration depths of available observational data. The enthalpy is calculated as the sum of the energy requirements for warming the sediment column to its freezing temperature and for thawing of the ice (Nicolsky & Romanovsky, 2018) and indicates the energy required to reach a permafrost-free sediment column.

To evaluate sensitivity of model output to parameterization, four grid cells were selected (see supporting information Table S1 and Figure 1) from the Beaufort and Western Laptev seas. The selected sites represent the full ranges of relative transgressive/regressive sedimentation regimes, and of subaerial/ submarine surface forcing. At these sites we varied (i) the model parameterization, (ii) the initial conditions, and (iii) the forcing data, as listed in the supporting information (Table S2) for 450 ka. We then analyzed how these variations changed the modeled lower permafrost boundary (i.e., 0 °C isotherm).

3. Results

3.1. Circumarctic Submarine Permafrost Distribution

Submarine permafrost evolution was simulated using vertical conductive heat flux for the Arctic shelf region with modern elevations between 150 and 0 m bsl and linear sedimentation rates for regressive and transgressive regimes of 10 and 30 cm/ka, respectively, mineral conductivity of 3 W·m^{-1}·K^{-1}, and initialization with

Table 1
Distribution of Shelf Areas and Regions Underlain by Cryotic Sediment Categorized Using a Modified Preliminary Classification of the Arctic Shelf Seas (International Hydrographic Organization, IHO, 2002)

Arctic Ocean region name	IHO area (in 10^6 km^2)	Modeled area (km^2)	Cryotic area (%)	Submarine permafrost (km^2)	Depth of 0° mean (range) (m)
Baffin Bay	—	55,900	26	7,700	290 (1–851)
Barents Sea	1.450	484,100	57	122,200	123 (1–623)7
Beaufort Sea	0.458	138,800	94	97,000	148 (31–841)
Chukchi Sea	0.373	516,600	99	472,800	171 (39–587)
Davis Strait	0.832	67,200	4	600	71 (51–187)
Greenland Strait	0.183	14,800	9	0	45 (27–61)
East Siberian	0.950	901,300	98	810,600	336 (39–927)
Greenland Sea	0.934	102,700	13	3,000	53 (1–299)
Hudson Bay	0.960	0	—	—	—
Hudson Strait	0.227	0	—	—	—
Iceland Sea	0.429	0	—	—	—
Kara Sea	0.937	623,600	89	434,700	381 (39–881)
Laptev Sea	0.669	468,400	98	402,700	420 (23–903)
Lincoln Sea	0.040	24,400	47	6,400	212 (1–767)
NW Passage	1.755	571,400	24	80,900	185 (1–1117)
Norwegian Sea	1.392	41,900	16	2,300	70 (19–179)
White Sea	0.096	65,200	74	18,600	71 (39–193)
Circumarctic	—	411,4500	75	2,483,100	287 (1–1117)

equilibrium conditions at 50 ka BP for a subset of cross-shelf transects. The resulting preindustrial spatial distribution of submarine permafrost and the depth of the 0 °C isotherm below the seafloor are shown in Figure 4. Submarine permafrost in Figure 4 is cryotic sediment that was exposed subaerially at some point during the past 450 ka and that exceeds the penetration depth of the 0 °C isotherm under modern assumed benthic temperatures (Figure 3), with a tolerance of 50 m. The latter condition excludes Holocene permafrost at the sea bed at temperatures higher than the freezing point of sea water (the region so excluded is shown in Figure 4). Submarine permafrost is unevenly distributed around the circumpolar shelf, with almost all modeled cryotic sediment distributed on the shelf east of 60°E and west of 120°W. Within each shelf sea, the cryotic permafrost thickness was generally greatest at the most recently submerged region, usually at the coast, and decreased northward toward the shelf edge (Figure 4).

Preindustrial submarine permafrost underlays more than 80% of five Arctic seas: the Beaufort, Chukchi, East Siberian, Laptev, and Kara Seas (Table 1). Of these the Kara, Laptev, and East Siberian Seas also have mean permafrost thicknesses exceeding 300 m bsf. Thus, the greatest spatial extent of permafrost underlies this region, which, together with the adjacent Chukchi Sea, comprises more than 60% of the modeled region. In the Canadian Arctic Archipelago, which includes the Lincoln Sea, Baffin Bay, part of the Davis Strait, and the Northwest Passages (Figure 1), modeled permafrost underlay 23% of the modeled region, and 5% of the shelf sea region. Grid cells with permafrost in the Canadian Arctic Archipelago, with the exception of the Beaufort coast (which is included in the Beaufort Sea region), were located adjacent to the coast. A similar distribution was found in the Barents Sea, where cryotic sediments underlay 57% of the modeled region (restricted to water depths of maximally 150 m), but only 19% of the sea's total area. Cryotic sediment in the Barents Sea was located primarily in two regions: south of Svalbard and along the coast, from around the Kanin Peninsula in the west to Novaya Zemlya. In the Kara Sea, permafrost distribution was strongly skewed toward the eastern portion of the sea, including Baydaratskaya Bay, a narrow strip less than 100 km wide along the western coast of the Yamal Peninsula, and the region northeastward toward Severnaya Zemlya. Contiguous regions with permafrost exceeding 500 m bsf in thickness were restricted to this portion of the Kara Sea, the Laptev Sea, and portions of the East Siberia Sea surrounding the New Siberian Islands.
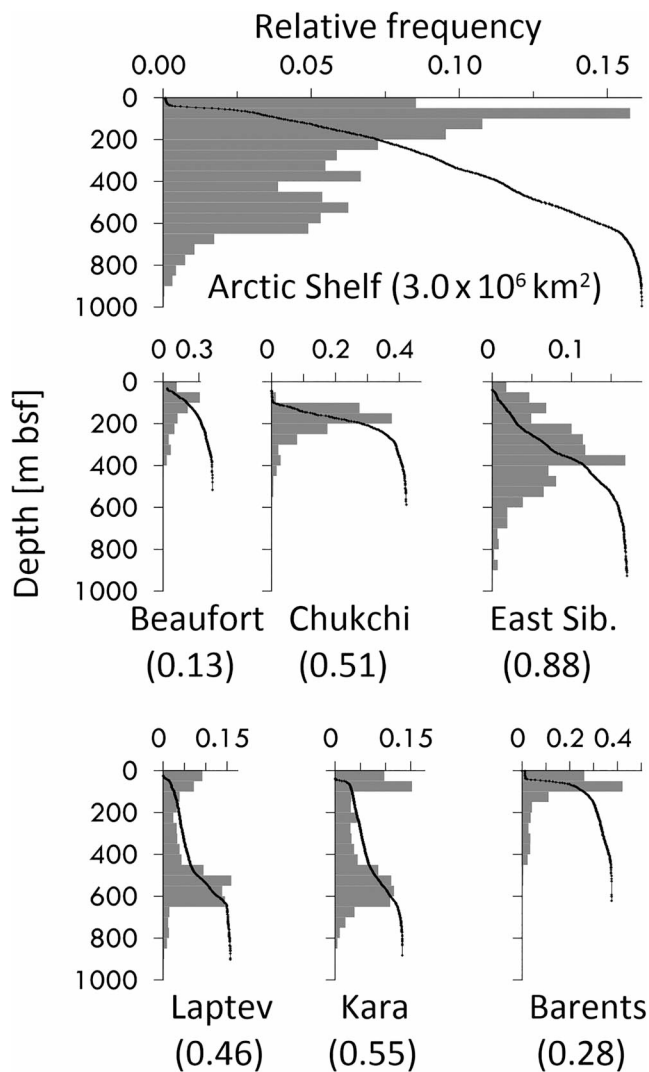
Figure 5. Histograms show the relative frequency of grid cells with cryotic sediment within the main Arctic shelf seas classified by the depth of the lower permafrost boundary beneath the sea floor. The x axes of the histograms are scaled proportionally to the number of grid cells so that the histogram areas are comparable. The area of cryotic sediment modeled within each shelf sea (in 10^6 km^2) are indicated in parentheses.

3.2. Permafrost Thickness

Figure 5 shows histograms of the depth of the lower 0°C isotherm below the seafloor for the Arctic shelf and for six of the shelf seas. Assuming that cryotic sediments extend from the seabed to this lower depth, hypsometric curves describe the cumulative exceedance functions for each shelf sea. Cryotic sediment was generated between 0 and 1,117 m bsf (depth of 0 °C isotherm). Half of the values lay between 160 and 470 m bsf (Figure 5), with a mean depth of cryotic sediment of 287 m bsf. For the Arctic shelf, the most frequent permafrost thickness was less than 200 m, but for individual seas, distributions of thickness varied. The seas accounting for the greatest area of the modeled permafrost (Kara, Laptev, and East Siberian) had peaks of permafrost thickness at greater depths (around 600, 600, and 400 m, respectively) than the other shelf regions. The depth of the 0 °C isotherm was shallow (<100 m bsf) in the Svalbard region and in the southeastern Barents Sea, except at its easternmost extent in Varandey Bay, where it exceeded 250 m bsf and where the IPA map also indicates a small region of submarine permafrost. Modeled submarine permafrost reached its greatest depth (1,117 m bsf) in the Canadian Arctic Archipelago.

Model sensitivity to variation of input parameters was tested for individual parameters with lower permafrost boundary depths of 255, 617, 601, and 541 m bsf at the Beaufort Sea and western Laptev Sea sites, respectively. The depth to the lower boundary of cryotic sediment changed by more than 100 m for imposed changes in two parameters only: subaerial forcing temperature (varied by ±5 °C) and sediment mineral thermal conductivity (from −67% to 233%). Decreasing air temperatures uniformly by 5 °C increased permafrost thicknesses by 78% and 32% to 37%, for the Beaufort and the three western Laptev sites, respectively. An increase in mineral thermal conductivity from 3 to 5 W/m resulted in 170 m (67%) thicker permafrost at the Beaufort site and 300 to 350 m (around 55%) at the western Laptev sites. For all other parameters (sea level: ±40 m, sedimentation rate: 10–60 cm/ka, depositional regime: 0–100% marine, marine sediment salinity: ±10%, porosity: ±30%, subglacial forcing: −5 to 0 °C, and geothermal heat flux: ±10%), changes were less than 100 m (see supporting information Table S2).

3.3. Permafrost Temperature and Temporal Variability

For particular transects extending northward from the coast, we describe model results for the temporal development of modeled submarine permafrost for 2-D cross sections of the shelf. Results give insights into (i) the behavior of the model, (ii) the dependence of submarine permafrost extent and composition on transient forcing, and (iii) the importance of modeled processes in determining modern permafrost distribution. Transects were chosen to reflect the diversity of paleoenvironmental histories around the Arctic shelf and to correspond to previous modeling efforts and/or potential observational data sets. Table 2 lists the transects and their characteristics, as well as any references with similarly located modeling or observational results.

Figure 6 shows modeled modern temperature and ice content distribution as a function of lateral distance from the coast with modern bathymetry and elevation. The profiles presented here run northward from onshore positions, where terrestrial permafrost (at left in each profile) gives an indication of pretransgression permafrost temperature, thickness, and ice content. The profiles extend out to 150-m water depth. The Harrison Bay (HB) and Camden Bay (CB) profiles transect the Alaskan Beaufort coastline, where Ruppel et al. (2016) analyze borehole records. The Mackenzie (MP) profile transects the Canadian Beaufort coastline 140 km northeast of Tuktoyaktuk and extends more than 150 km offshore, where Taylor et al. (2013) model permafrost evolution. The central Laptev Sea (CL) profile was located just east of the Lena Delta

Table 2
Transects of Permafrost Modeled for 450 ka Across the Arctic Shelf Presented in This Study, Chosen to Correspond to Results From Existing Studies of Submarine Permafrost (Figure 1)

Transect	Longitude	Latitude range	Reference
Camden Bay	145°W	69.7–70.765°N	Ruppel et al. (2016)
Harrison Bay	150°W	70.3–71.225°N	Ruppel et al. (2016)
Mackenzie	134°W	69.0–71.1°N	Taylor et al. (2013)
Central Laptev	130°E	70.98–77.8°N	Nicolsky et al. (2012)

where the shelf extends over 800 km northward from the coastline. Animations of sediment temperature and ice saturation as a function of time are available in the supporting information.

Sediment temperature along the profiles and down to a depth of 1 km bsl ranged from −10 to over 20 °C. Modeled ice saturation of the sediment pore space varied between 0 for sediment with temperature above T_f up to near 1 (complete saturation) for cold terrestrial sediment strata. Sediment temperatures were blocky, reflecting the coarse spatial resolution of the modeled ice cap distribution provided by the CLIMBER-2 model, which lead to step-like changes in temperature and the lower boundary of ice bearing permafrost along the profile. The depth of the 0 °C isotherm along the submarine portions of HB, CB, and MP lay between 100 and 300 m bsl except distal to the coast at HB and CB, where it reached a maximum depth of 500 and 450 m bsl, respectively. Sediment temperatures were greater than −1 °C throughout the vertical profile, that is, had reached near isothermal conditions, not more than 20 km from the coastline. Along the Laptev Sea profile, transgression of permafrost more than 700 m thick resulted in submarine permafrost with temperatures between 0 and −2 °C. Toward the shelf edge for all profiles, surface sediments were cooled by cold bottom waters to temperatures between −1 and −2 °C, visible here as the introduction of and increasing depth of the −1 °C isotherm. The CL profile transects Muostakh Island at about 50 km northward of the coastline. At this location, subaerial exposure resulted in modeled permafrost temperatures below −8 °C.

3.4. Ice Content and Saturation

The ice saturation of the sediment pore space is a function of sediment grain size and compaction, pore water salinity, and the heat flux history of each grid cell. Sediment temperature gives some indication of permafrost state, but the latent heat of thawing of any ice present is responsible for the thermal inertia of the permafrost. This thermal inertia contributes to the longevity of the gas hydrate stability zone present within and below much of the permafrost on the shelf (Romanovskii et al., 2004). Furthermore, the function of submarine permafrost as a barrier to gas migration is a result of gas diffusivities that are orders of magnitude lower in ice-bonded permafrost than in ice-free sediment (Chuvilin et al., 2013). Of the modeled region of 4.1×10^6 km^2, 75% were cryotic, but mean ice contents (averaged over the IHO sea regions) in the sediment column were less than 130 m^3/m^2, with a maximum modeled ice content at any one location of 191 m^3/m^2. The distribution of total ice contents was similar to values for the depth of the 0 °C isotherm, that is, heavily skewed toward low values. Mean ice contents and permafrost thicknesses increased in the Barents, Beaufort, Chukchi, Kara, East Siberian, and Laptev Seas, successively (supporting information Figure S4). Toward the shelf edge in each profile water depth increased, as did the duration of modeled marine sedimentation. Transgressive strata increased in thickness as well, lowering the sediment column ice content. Ice saturation in the profiles reflected the temperature distribution and the onlapping of transgressive sediment, whose salinity lowered the sediment pore water freezing temperature and pore space ice saturation (Figure 6).

4. Discussion

SuPerMAP models 1-D heat conduction and applies global to circumarctic spatial scale input data for its boundary conditions to generate a distribution of cryotic sediment and ice content on the Arctic shelf. Permafrost present/absence and extent was similar to that predicted by the IPA map (Brown et al., 2001) at the scale of the Arctic seas. The modeled submarine permafrost region represents an area slightly larger than the area defined by the IPA map (Figure 4). In the largest contiguous region with deep permafrost, the East Siberian shelf, the distribution of permafrost resembles modeling efforts by Nicolsky et al. (2012) and Romanovskii et al. (2004) insofar as the majority of the shelf is underlain by permafrost several hundred
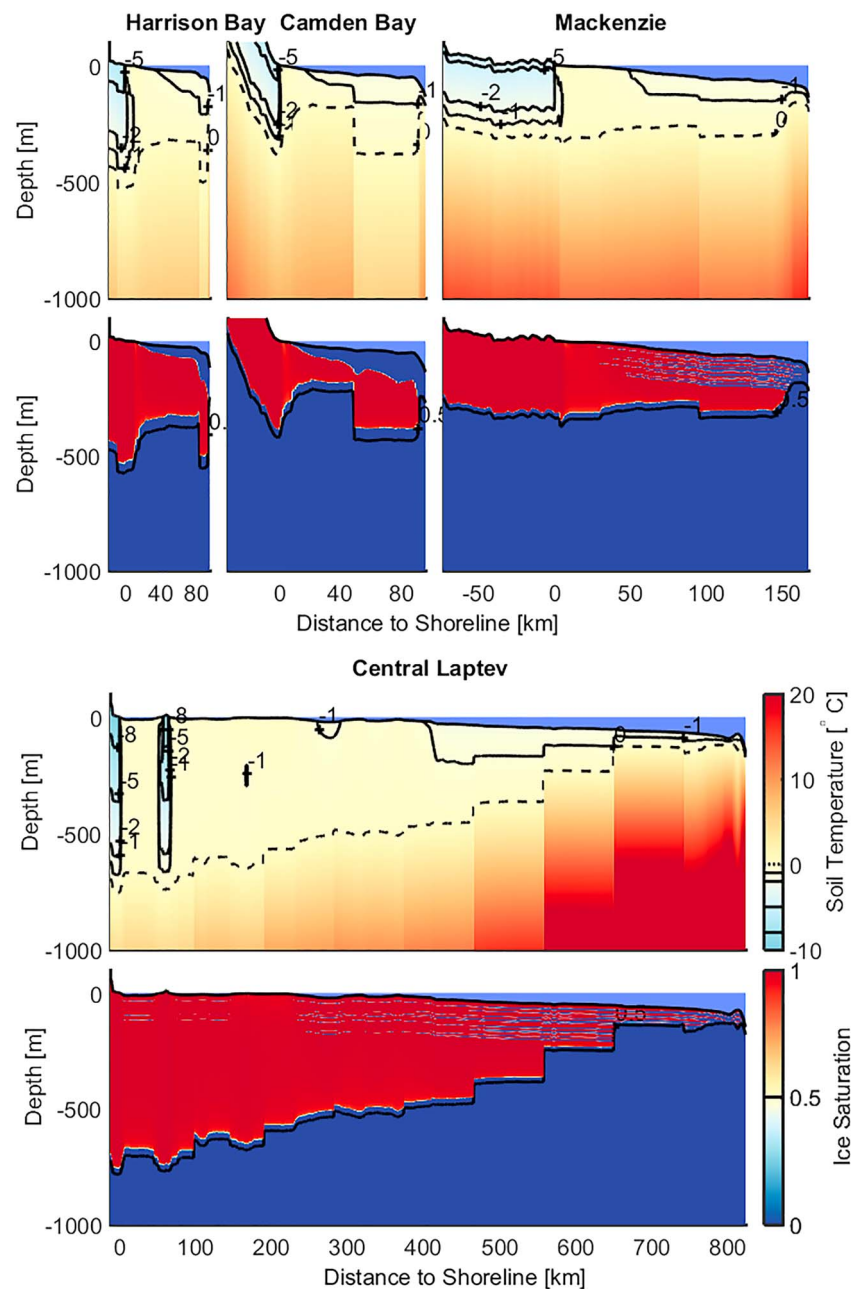
Figure 6. Modeled temperature field and ice saturation of four transects: Harrison Bay and Camden Bay, Beaufort Shelf (Mackenzie), and Central Laptev Sea. The locations were chosen to match existing observational or modeling studies (Table 2). Animations of surface forcing, sediment temperature, and ice saturation are available in the supporting information.

meters thick. This reflects a similarity in modeling approaches: Nicolsky extended Romanovskii's modeling by including the effect of liquid water content and surface geomorphology, and by considering the effect of an entirely saline sediment stratigraphy. Our model explicitly includes the effects of salt on the freezing curve, an implementation of sediment stratification, distributed geothermal heat flux, surface temperatures, ice sheet dynamics, and sea level rise over multiple glacial cycles, and is applied to the entire Arctic shelf.

Most of the modeled permafrost is relict, that is, it formed subaerially, was subsequently transgressed, and is consequently warming and thawing under submarine boundary conditions. Our model preserves cryotic sediment at the sea bed since benthic temperatures are maximally 0 °C. Thawing in this case occurs from below as a result of geothermal heat flux. Animations of the development of the permafrost (online

supporting information) demonstrate the modeled dynamics of freezing and thawing sediment. The sediment column generally approached isothermal conditions within 2 millenia of being either inundated or glaciated but remained cryotic, thawed from below by geothermal heat flux. Based on our model time step of 100a and output depth digitalization of 2 m, we have a resolution for permafrost thickness change rate of 0.02 m/a. At the end of the modeled period, 63% of our modeled region of cryotic sediment was not changing in thickness, whereas 36% was thinning at rates between −0.15 and −0.02 m/a and less than 1% was growing in thickness under preindustrial forcing conditions. Fitting linear trends to the 500-year period prior to industrial time yielded 2.8% of the permafrost area with aggrading permafrost, while 97.2% of the region was warming. Onlapping transgressive sediment layers remained comparatively ice free due to the lowering of the pore water freezing temperature. At any inundated or glaciated location, the duration of warming and the proportion of the sediment column that was saline most strongly influenced the depth of the 0 °C isotherm and the total sediment column ice content.

Simplifications in our model parameterization lead to either underestimation or overestimation of permafrost extent. Our model does not include thawing from above via the infiltration of saline benthic water into the seabed (e.g., Harrison, 1982), which Angelopoulos et al. (2018) suggest occur at rates of less than 0.1 m/a over decadal time scales. Razumov et al. (2014) adopt even lower degradations of less than 80 m for the western Laptev Sea shelf. Benthic temperatures around the gateways between the Arctic and the rest of the world ocean are warmed by inflowing water, as is also the case in estuary and river mouth regions. For example, bottom water temperatures measured in 2012–2013 on the Barents shelf were not less than −2 °C (e.g., Eriksen, 2012), and positive almost everywhere, due to the influence of mixing and inflowing Atlantic waters. The effect of warmer Atlantic waters at the shelf edge are observed as far as the Laptev Sea shelf (Janout et al., 2017) and the Chuckhi Sea shelf (Ladd et al., 2016). The Chukchi shelf bottom waters are influenced by waters bringing heat into the Arctic Ocean through the Bering Strait (Woodgate, 2018). By ignoring isostasy, regions of glacio-isostatic rebound may be classified as subaerial, due to their higher modern elevation, during periods of glaciation and deglaciation. This results in colder forcing than would be true at the sea floor, or even subglacially, and thus the development of permafrost. Both effects lead to an overestimation of the areal extent of cryotic sediments. On the other hand, uncertainties in glacial coverage and subglacial temperatures, especially since the Last Glacial Maximum, have a strong effect on modeled modern permafrost thickness. Recent evidence of grounded ice (Farquharson et al., 2018) and of ice caps on the East Siberian Shelf (Gasson et al., 2018; Niessen et al., 2013) suggest a greater ice cap extent history than previously accepted, which would lead to shallower permafrost depths.

4.1. Comparison to Observation

Existing data sets for comparison with model output exist where geophysical survey or borehole data are publicly available. The former are usually seismic or electromagnetic surveys. To detect permafrost, seismic analyses identify increases in bulk compressional wave velocity of sediments, which generally only increase once ice content exceeds 0.4. Geophysical borehole logs provide greater detail about the vertical distribution of permafrost-bearing sediments but only for discrete locations. Electrical resistivity logs are the most useful for identifying and distinguishing intact permafrost, layers with thawing permafrost, and sediments lacking ice (e.g., Ruppel et al., 2016). Recent work using controlled source electromagnetics in shallow waters gives an indication of the thicknesses of permafrost and its distribution (Sherman et al., 2017). Boreholes are useful for validation when they are deep enough to penetrate subsea permafrost, restricting them to exploration and industry wells. Scientific studies of subsea permafrost on the eastern Siberian shelf are available (e.g., Fartyshev, 1993; Kassens et al., 2007; Kunitsky, 1989; Melnikov et al., 1985; Molochushkin, 1970; Schirrmeister, 2007; Slagoda, 1993; Soloviev et al., 1987) but describe surface sediment samples and boreholes shallower than 100 m below the sea floor. For the U.S. Beaufort shelf, Brothers et al. (2016) and Ruppel et al. (2016) collect all available seismic and borehole data to explore the distribution of permafrost.

The comparatively steep shelves of the Beaufort are erosional, and Holocene sediments are absent out to the 30-m isobaths (Are, 1994; Reimnitz et al., 1982). In contrast, sediments east of the Mackenzie river were assumed to be mostly the result of postglacial sediment or buried morainic material and nonsaline (Batchelor et al., 2013). For comparison of model output with published permafrost extents for the narrow Alaskan Beaufort shelf, marine sedimentation only was modeled for the Alaskan Beaufort shelf (Figure 7), whereas both marine and terrestrial sedimentation were modeled for the Canadian Beaufort shelf, as for the circumarctic case (east of 138°W). For the Beaufort case, the increased salinity (i.e., more transgressive sediment in the profile) renders modeled permafrost thickness more sensitive to porosity, although varying the
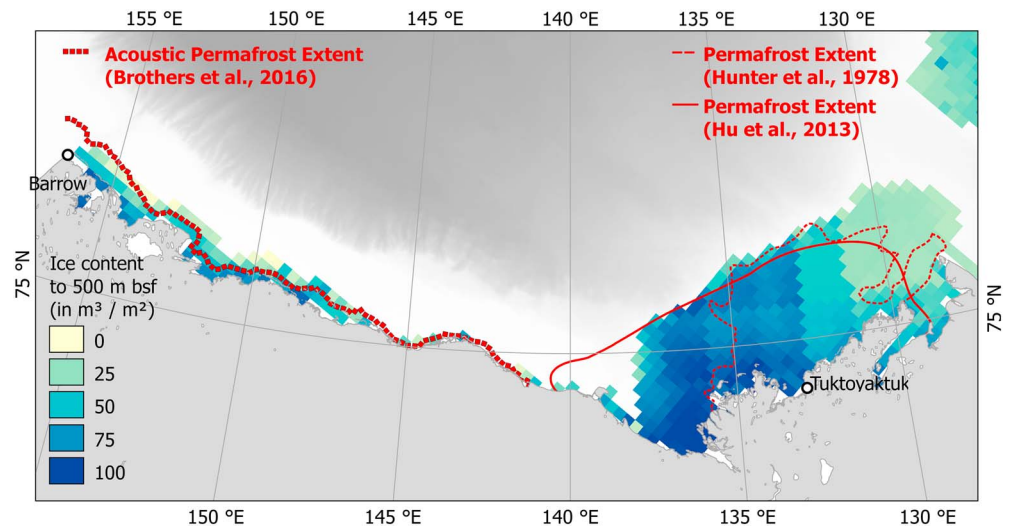
Figure 7. Comparison of model output, in this case, ice content in the uppermost 500 m of the sediment column beneath the sea floor (m^3/m^2), to the extent of seismically delineated permafrost reported in Ruppel et al. (2016), to the west, and to the permafrost extent published in Hunter et al. (1978) and Hu et al. (2013), to the east. Hunter et al., 1978's (1978) distribution has been updated by Hu et al. (2013) through reinterpretation of industry borehole records.

salinity of the transgressive sediment layers has little to no effect on the depth of the 0 °C isotherm (Table S2). The seismic and borehole permafrost delineation of Ruppel et al. (2016) matches within two EASE grid cells of the modeled ice content values for the upper sediment column, which matches the depth of investigation of seismic data evaluation in Brothers et al. (2016). Modeled isothermal sediment temperatures out to maximally 20 km from the coastline suggest a narrow region of cryotic sediments that contain thawing ice. Comparison of the permafrost delineation offshore of the Mackenzie mouth (Hunter et al., 1978) and modeled ice content give poor agreement. The Mackenzie outflow has warmer benthic temperatures than used as boundary condition in the model (Stevens et al., 2010), leading to an overestimation of permafrost ice content to the west within the Canadian Beaufort sector. The underestimation of permafrost ice content to the east may result from local inaccuracies in modeled glacial dynamics from CLIMBER-2 or in sediment thermal properties. On the Alaskan side of the Beaufort shelf, these results suggest that permafrost submarine
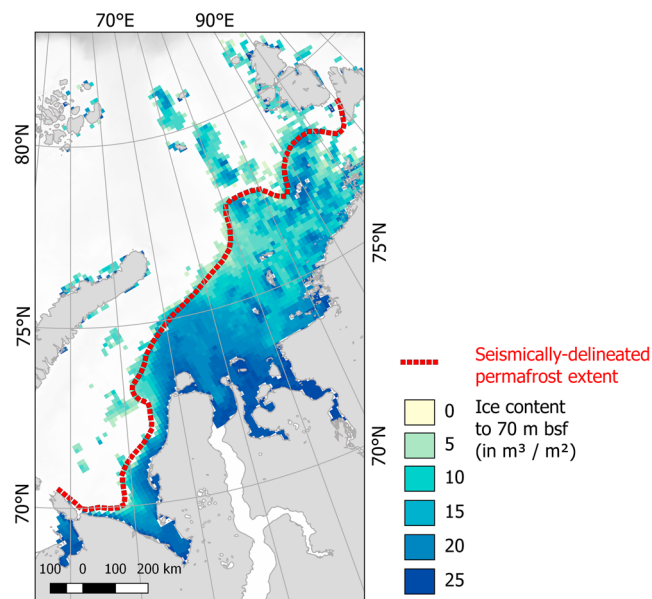

Figure 8. Comparison of model output, in this case ice content (m^3/m^2) for the uppermost 70 m of the modeled sediment column, to the extent of seismically delineated permafrost reported in Rekant and Vasiliev (2011).

degradation is either faster than has been assumed, or that conditions before transgression preconditioned permafrost by warming, when compared to permafrost on the Siberian shelf.

On the Kara Sea shelf, geotechnical results including records from 16 boreholes in coastal areas provide poor constraint for permafrost distribution (Melnikov & Spesivtsev, 1995; Vasiliev et al., 2018). Rekant et al. (2015) use high-resolution seismic methods to detect acoustic permafrost as high-amplitude reflections based on the difference in propagation velocities of the acoustic signal at the frozen/unfrozen boundary (Niessen et al., 1999). The delineation of permafrost extent in the Kara sea is based on seismic studies using a Sonic M141 seismoacoustic subbottom profiler operating at 1.4–14 kHz and 10 kW output power with a penetration depth of about 70 m. The 30,000 km of seismic profiles were collected and the occurrence of seismically delineated permafrost mapped (Rekant et al., 2015). Seismic detection of permafrost was compared to drilling results along a 12-km profile at Cape Kharasavey offshore of Western Yamal. Permafrost was limited to measurements in water depths of less than 114 m. The resulting delineation is compared to permafrost ice content in the upper 70 m of the sediment column in Figure 8, based on modeling using the same sedimentation rates assumed for the circumarctic case.

5. Conclusion

Modeling of heat conduction below the land surface and below the Arctic shelf provides an estimate of permafrost development north of 65°. The simulation was based on dynamic boundary conditions from above, including four glacial cycles of air temperature, glacial ice coverage and sea level variation, and distributed geothermal heat flux from below. Sediment stratigraphy accounts for regressive and transgressive sedimentation in a manner consistent around the circumarctic shelf. Model output suggested extensive preindustrial cryotic sediment distribution of about $2.5 \times 10^6 km^2$, more than 80% of which is located beneath the Siberian shelves. These cryotic sediments are mostly warming and thawing and more than 97% of the submarine permafrost modeled is thinning. Ice content in submarine permafrost is <200 m^3/m^2. Comparison to seismically delineated permafrost on the Alaskan Beaufort shelf and in the Kara Sea show reasonable agreement with modeled ice contents. Comparison to borehole records from the Mackenzie Delta region shows discrepancies with modeled distribution and depth. Model sensitivity to input parameters suggests that improvements to the representation of sediment thermal properties, sedimentation and erosion and to surface forcing offer the most effective way to improve the model. Future model implementations will include solute diffusion in the sediment column to simulate permafrost thaw beneath the seabed and improve the spatial and temporal distribution of sedimentation and erosion. A 1-D transient heat flow model provides a reasonable first-order estimate of submarine permafrost distribution on the Arctic shelf.

References

Angelopoulos, M., Westermann, S., Overduin, P., Faguet, A., Olenchenko, V., Grosse, G., & Grigoriev, M. N. (2018). Heat and salt flow in subsea permafrost modelled with CryoGRID2. *Journal of Geophysical Research: Earth Surface*. https://doi.org/10.1029/2018JF004823

Anisimov, O. A., Zaboikina, Y. G., Kokorev, V. A., & Yuganov, L. N. (2014). Possible causes of methane release from the East Arctic seas shelf. *Ice and Snow*, *126*, 69–81. https://doi.org/10.15356/2076-6734-2014-2-69-81

Are, F. E. (1994). Dynamics of the littoral zone of Arctic Seas (state of the art and goals). *Polarforschung*, *64*, 123–131.

Are, F. E. (2003). Shoreface of the Arctic seas—A natural laboratory for subsea permafrost dynamics. In M. Philips, S. M. Springman, & L. U. Arenson (Eds.), *Proceedings of the eighth international conference on permafrost, Zürich, Switzerland* (pp. 27–32). Lisse: Swets & Zeitlinger.

Batchelor, C. L., Dowdeswell, J. A., & Oietras, J. T. (2013). Seismic stratigraphy, sedimentary architecture and palaeo-glaciology of the Mackenzie Trough: Evidence for two Quaternary ice advances and limited fan development on the western Canadian Beaufort Sea margin. *Quarternary Science Reviews*, *65*, 73–87. https://doi.org/10.1016/j.quascirev.2013.01.021

Bauch, H. A., Mueller-Lupp, T., Taldenkova, E., Spielhagen, R. F., Kassens, H., Grootes, P. M., et al. (2001). Chronology of the Holocene transgression at the North Siberian margin. *Global and Planetary Change*, *31*(1–4), 125–139. https://doi.org/10.1016/S0921-8181(01)00116-3

Bittelli, M., Flury, M., & Campbell, G. S. (2003). A thermodielectric analyzer to measure the freezing and moisture characteristic of porous media. *Water Resources Research*, *39*(2), 1041. https://doi.org/10.1029/2001WR000930

Blasco, S. M., Fortin, G., Hill, P. R., O'Connor, M. J., & Brigham-Grette, J. (1990). The late Neogene and Quaternary stratigraphy of the Canadian Beaufort continental shelf. In A. Grantz, L. Johnson, & J. F. Sweeney (Eds.), *The geology of North America, The Arctic Ocean Region* (Vol. L, pp. 491502). Boulder, CO: Geol. Soc. of Am. https://doi.org/10.1130/DNAG-GNA-L.491

Blasco, S., Jenner, K., Davies, E., Michel, F., Pollard, W., Graham, C., & Ruffell, R. (2012). Origin and evolution of subsea ice-bearing permafrost on the Canadian Beaufort shelf: Implication from a 500 m deep borehole. In *Proceedings of tenth international conference on permafrost, extended abstracts* (Vol. 4, pp. 56). Salekhard, Yamal-Nenets Autonomous District, Russia: The Northern Publisher (Severnoye Izdatelstvo). https://doi.org/10.1002/2016GC006582

Boulton, G. S. (1996). Theory of glacial erosion, transport and deposition as a consequence of subglacial sediment deformation. *Journal of Glaciology*, *140*, 43–62. https://doi.org/10.3189/S0022143000030525

Brigham-Grette, J., & Hopkins, D. M. (1995). Emergent marine record and paleoclimate of the Last Interglaciation along the northwest Alaskan coast. *Quaternary Research*, *43*(2), 159–173. https://doi.org/10.1006/qres.1995.1017

Brodzik, M. J., Billingsley, B., Haran, T., Raup, B., & Savoie, M. H. (2012). EASE-Grid 2.0: Incremental but significant improvements for earth-gridded data sets. *ISPRS International Journal of Geo-Information*, *1*(1), 32–45. https://doi.org/10.3390/ijgi1010032

Brodzik, M. J., Billingsley, B., Haran, T., Raup, B., & Savoie, M. H. (2014). Correction: Brodzik et al. EASE-Grid 2.0: Incremental but Significant Improvements for Earth-Gridded Data Sets. *ISPRS International Journal of Geo-Information*, *3*(3), 1154–1156. https://doi.org/10.3390/ijgi1010032

Brothers, L. L., Herman, B. M., Hart, P. E., & Ruppel, C. D. (2016). Subsea ice-bearing permafrost on the U.S. Beaufort Margin: 1. Minimum seaward extent defined from multichannel seismic reflection data. *Geochemistry, Geophysics, Geosystems*, *17*, 4354–4365. https://doi.org/10.1002/2016GC006584

Brown, J., Ferrians, O. J. J., Heginbottom, J. A., & Melnikov, E. S. (2001). *Circum-Arctic map of permafrost and ground-ice conditions*. Washington, D. C.: U.S. Geological Survey in Cooperation with the Circum-Pacific Council for Energy and Mineral Resources. https://doi.org/10.3133/cp45

Chuvilin, E. M., Bukhanov, B. A., Tumskoy, V. E., Shakhova, N. E., Dudarev, O. V., & Semiletov, I. P. (2013). Thermal conductivity conductivity of bottom sediments in the region of Buor-Khaya Bay (shelf of the Laptev Sea). *Earth Cryosphere*, *17*(2), 32–40.

Dall'Amico, M., Endrizzi, S., & Rigon, R. (2011). A robust and energy-conserving model of freezing variably-saturated soil. *The Cryosphere*, *5*, 169–484. https://doi.org/10.5194/tc-5-469-2011

Dallimore, S. R. (1991). Geological, geotechnical and geophysical studies along an onshore-offshore transect of the Beaufort Shelf. *Geological Survey of Canada, Open File*, *2408*, 325. https://doi.org/10.4095/132227

Dallimore, S. R., & Collett, T. S. (1995). Intrapermafrost gas hydrates from a deep core hole in the Mackenzie Delta, Northwest Territories, Canada. *Geology*, *23*(6), 527–530. https://doi.org/10.1130/0091-7613(1995)023<0527:IGHFAD>2.3.CO;2

Davies, J. H. (2013). Global map of solid Earth surface heat flow. *Geochemistry, Geophysics and Geosystems*, *14*, 15. https://doi.org/10.1002/gggc.20271

Dmitrenko, I. A., Kirillov, S. A., Tremblay, L. B., Kassens, H., Anisimov, O. A., Lavrov, S. A., et al. (2011). Recent changes in shelf hydrography in the Siberian Arctic: Potential for subsea permafrost instability. *Journal of Geophysical Research*, *116*, C10027. https://doi.org/10.1029/2011JC007218

Eriksen, E. (2012). Survey report from the joint Norwegian/Russian ecosystem survey in the Barents Sea august-october 2012. Institute of Marine Research (IMR), Bergen, Norway & Nikolai M. Knipovich Polar Research Institute of Marine Fisheries and Oceanography (PINRO).

Farquharson, L., Mann, D., Rittenour, T., Groves, P., Grosse, G., & Jones, B. (2018). Alaskan marine transgressions record out-of-phase Arctic Ocean glaciation during the Last Interglacial. *Geology*, *46*, 783–786. https://doi.org/10.1130/G40345.1

Fartyshev, A. I. (1993). *Osobennosti Priberezhno-Shelfovoi Kriolitozony Morya Laptevykh (characteristics of the near-shore Laptev Sea Shelf) Edited by* N. N. Romanovskii. Siberian Branch, Nauka, Novosibirsk: Russian Academy of Sciences.

Forbes, D. L., Manson, G. K., Whalen, D. J. R., Couture, N. J., & Hill, P. R. (2015). Coastal products of marine transgression in cold-temperate and high-latitude coastal-plain settings: Gulf of St Lawrence and Beaufort Sea. In I. P. Martini & H. R. Wanless (Eds.), *Sedimentary coastal zones from high to low latitudes: Similarities and differences* (pp. 33). London: Geological Society, London, Special Publications.

Frederick, J. M., & Buffett, B. A. (2015). Effects of submarine groundwater discharge on the present-day extent of relict submarine permafrost and gas hydrate stability on the Beaufort Sea continental shelf. *Journal of Geophysical Research: Earth Surface*, *120*, 417–432. https://doi.org/10.1002/2014JF003349

Ganopolski, A., Calov, R., & Claussen, M. (2010). Simulation of the last glacial cycle with a coupled climate ice-sheet model of intermediate complexity. *Climate of the Past*, *6*, 229–244. https://doi.org/10.5194/cp-6-229-2010

Gasson, E. G. W., DeConto, R. M., Pollard, D., & Clark, C. D. (2018). Numerical simulations of a kilometre-thick Arctic ice shelf consistent with ice grounding observations. *Nature Communications*, *9*, 5910. https://doi.org/10.1038/s41467-018-03707-w

Grant, K. M., Rohling, E. J., Bronk Ramsey, C., Cheng, H., Edwards, R. L., Florindo, F., et al. (2014). Sea-level variability over five glacial cycles. *Nature Communications*, *5*(5076), 9.

Gross, M. G. (1977). *Oceanography: A view of the Earth* (2nd ed.). Englewood Cliffs, NJ: Prentice-Hall, Inc.

Gu, X., Tenzer, R., & Gladkikh, V. (2014). Empirical models of the ocean–sediment and marine sediment–bedrock density contrasts. *Geosciences Journal*, *18*(4), 139–447. https://doi.org/10.1007/s12303-014-0015-9

Hamilton, E. L. (1976). Variations of density and porosity with depth in deep-sea sediments. *Journal of Sedimentary Research*, *46*(2), 280–300. https://doi.org/10.1306/212F6F3C-2B24-11D7-8648000102C1865D

Harrison, W. D. (1982). Formulation of a model for pore water convection in thawing subsea permafrost. *Mitteilungen der Versuchsanstalt für Wasserbau, Hydrologie und Glaziologie*, *57*, 3–24.

Harrison, W. D., & Osterkamp, T. E. (1982). Environmental assessment of the Alaskan continental shelf. In *Annual reports of principal investigators for the year ending March 1977, Volume XVII. Hazards, Outer Continental Shelf Environmental Assessment Program (OSCEAP)* (pp. 424–510). Boulder, CO: National Oceanic and Atmospheric Administration (NOAA).

Hartikainen, J., & Kouhia, R. (2010). Permafrost simulations at Forsmark using a numerical. 2D thermo-hydro-chemical model (TR-09-17). Stockholm. Retrieved from www.skb.se/upload/publications/pdf/TR-09-17.pdf

Hivon, E. G., & Sego, D. C. (1995). Strength of frozen saline soils. *Canadian Geotechnical Journal*, *32*(2), 336–354. https://doi.org/10.1139/t95-034

Hu, K., Issler, D. R., Chen, Z., & Brent, T. A. (2013). Permafrost investigation by well logs, and seismic velocity and repeated shallow temperature surveys, Beaufort-Mackenzie Basin. *Geological Survey of Canada, Open File*, *6956*, 33. https://doi.org/10.4095/293120

Hunter, J. A., Neave, K. G., MacAulay, H. A., & Hobson, G. D. (1978). Interpretation of sub-seabottom permafrost in the Beaufort Sea. In C. B. Crawford (Ed.) pp. 514–520). Canada: National Research Council of Canada.

International Hydrographic Organization (2002). Names and limits of oceans and seas (4th ed.). (*IHO PUBLICATION S-23*). Monaco: International Hydrographic Organization.

Issler, D. R., Hu, K., Lane, L. S., & Dietrich, J. R. (2013). GIS Compilations of depth to overpressure, permafrost distribution, geothermal gradient, and regional geology, Beaufort-Mackenzie Basin, Northern Canada. *Geological Survey of Canada, Open File*, *5689*, 1–11. https://doi.org/10.4095/289113

Jackson, H., & Oakey, G. (1990). Sedimentary thickness map of the Arctic Ocean. In A. Grantz, L. Johnson, & J. F. Sweeney (Eds.), *The Arctic Ocean region* (Vol. L, plate 5). Boulder, CO: Geological Society of America, The Geology of North America.

Jakobsson, M., Mayer, L., Coakley, B., Dowdeswell, J. A., Forbes, S., Fridman, B., et al. (2012). The International Bathymetric Chart of the Arctic Ocean (IBCAO) version 3.0. *Geophysical Research Letters*, *39*, L12609. https://doi.org/10.1029/2012GL052219

Janout, M. A., Hölemann, J., Timokhov, L., Gutjahr, O., & Heinemann, G. (2017). Circulation in the northwest Laptev Sea in the eastern Arctic Ocean: Crossroads between Siberian River water, Atlantic water and polynya-formed dense water. *Journal of Geophysical Research: Oceans*, *122*, 6630–6647. https://doi.org/10.1002/2017JC013159

Kassens, H., Bauch, H. A., Dmitrenko, I. A., Eicken, H., Hubberten, D. H. W., Melles, M., et al. (1999). *Land-ocean systems in the Siberian Arctic: Dynamics and history*. Berlin Heidelberg: Springer. https://doi.org/10.1007/978-3-642-60134-7

Kassens, H., Thiede, J., Bauch, H., Hoelemann, J. A., Dmitrenko, I., Pivovarov, S., et al. (2007). *The Laptev Sea system since the last glacial Edited by* H. Hauff, vol. Boulder, Colo., USA: Geological Society of America. https://doi.org/10.1130/2007.2426(06)

Kitover, D. C., van Balen, R. T., Vandenberghe, J., Roche, D. M., & Renssen, H. (2015). LGM permafrost thickness and extent in the Northern Hemisphere derived from the Earth System Model iLOVECLIM. *Permafrost and Periglacial Processes*, *12*, 31–42. https://doi.org/10.1002/ppp.1861

Kleiber, H. P., & Nissen, F. (2000). Variations of continental discharge pattern in space and time: Implications from the Laptev Sea continental margin, Arctic Siberia. *International Journal of Earth Sciences*, *89*, 605–616. https://doi.org/10.1007/s005310000130

Klein, L. A., & Swift, C. T. (1977). An improved model for the dielectric constant of sea water at microwave frequencies. *lEEE Transactions on Antennas and Propagation*, *25*, 104–111.

Kominz, M. A., Patterson, K., & Odette, D. (2011). Lithology dependence of porosity in slope and deep marine sediments. *Journal of Sedimentary Research*, *81*, 730–742. https://doi.org/10.2110/jsr.2011.60

Kunitsky, V. V. (1989). Kriolitologiya nizovya leny (Cryolithology of the Lower Lena). Melnikov Permafrost Institute, Russian Academy of Sciences, Siberian Branch, Yakutsk.

Kuptsov, V. M., & Lisitzin, A. P. (1996). Radiocarbon of Quarternary along shore and bottom deposits of the Lena and the Laptev Sea sediments. *Marine Chemistry*, *53*, 301–311. https://doi.org/10.1016/0304-4203(95)00096-8

Lachenbruch, A. H. (1957). Thermal effects of the ocean on permafrost. *Bulletin of the Geological Society of America*, *68*, 1515. https://doi.org/10.1130/0016-7606(1957)68[1515:TEOTOO]2.0.CO;2

Lachenbruch, A. H. (2002). Thermal effects of the ocean on permafrost. In A. S. Goudie (Ed.), *Encyclopedia of global change: Environmental change and human society* (Vol. 2, pp. 224–235). Oxford: Oxford University Press.

Ladd, C., Mordy, C. W., Salo, S. A., & Stabeno, P. J. (2016). Winter water properties and the Chukchi Polynya. *Journal of Geophysical Research: Oceans*, *121*, 5516–5534. https://doi.org/10.1002/2016JC011918

Lee, M. W. (2005). Well log analysis to assist the interpretation of 3-D seismic data at Milne Point (2005-5048). North Slope of Alaska. Retrieved from http://pubs.usgs.gov/sir/2005/5048/

Loch, J. P. G. (1978). Thermodynamic equilibrium between ice and water in porous media. *Soil Science*, *126*(2), 77–80.

Ma, W., Zhang, L., & Yang, C. (2015). Discussion of the applicability of the generalized Clausius -Clapeyron equation and the frozen fringe process. *Earth-Science Reviews*, *142*, 47–59. https://doi.org/10.1016/j.earscirev.2015.01.003

McGuire, A. D., Anderson, L. G., Christensen, T. R., Dallimore, S., Guo, L., Hayes, D. J., et al. (2009). Sensitivity of the carbon cycle in the Arctic to climate change. *Ecological Monographs*, *79*, 523–555. https://doi.org/10.1890/08-2025.1

Melnikov, P. I., Makarov, V. N., Romanov, V. P., & Tishin, M. I. (1985). *Hydrochemical, thermophysical and radiocarbon studies at the Laptev Sea Coast, report of the permafrost institute*. Yakutsk: Siberian Branch Russian Academy of Sciences.

Melnikov, V. P., & Spesivtsev, V. I. (1995). *Engineering-geological and geocryological conditions of the Barents and Kara Shelves (in Russian)*. Novosibirsk: Nauka.

Millero, F. J., Feistel, R., Wright, D. G., & McDougall, T. J. (2008). The composition of standard seawater and the definition of the reference-composition salinity scale. *Deep Sea Research Part I: Oceanographic Research Papers*, *55*(1), 50–72.

Molochushkin, E. (1970). Thermal regime of deposits in the Southeastern Laptev Sea (PhD thesis), Moscow State University, Moscow.

Murray-Wallace, C. V., & Woodroffe, C. D. (2014). *Quaternary sea-level changes: A global perspective*. Cambridge, UK: Cambridge University Press.

Nicolsky, D. J., & Romanovsky, V. E. (2018). Modeling long-term permafrost degradation. *Journal of Geophysical Research: Earth Surface*, *123*, 1756–1771. https://doi.org/10.1029/2018JF004655

Nicolsky, D. J., Romanovsky, V. E., Romanovskii, N. N., Kholodov, A. L., Shakhova, N. E., & Semiletov, I. P. (2012). Modeling sub-sea permafrost in the East Siberian Arctic Shelf: The Laptev Sea region. *Journal of Geophysical Research*, *117*, F03028. https://doi.org/10.1029/2012JF002358

Niessen, F., Gierlichs, A., Weigelt, E., & Jokat, W. (1999). High-resolution seismic and sediment echosounding investigation of submarine permafrost on the Laptev Sea shelf. *Terra Nostra*, *11*, 54–55.

Niessen, F., Hong, J. K., Hegewald, A., Matthiessen, J., Stein, R., Kim, H., et al. (2013). Repeated Pleistocene glaciation of the East Siberian continental margin. *Nature Geoscience*, *6*, 842–846. https://doi.org/10.1038/ngeo1904

Osterkamp, T. E. (2001). Sub-sea permafrost. In J. H. Steele, S. A. Thorpe, & K. K. Turekian (Eds.), *Encyclopedia of ocean sciences* (Vol. 5, pp. 2902–2912). New York, London: Academic Press.

Overduin, P. P., Liebner, S., Knoblauch, C., Günther, F., Wetterich, S., Schirrmeister, L., et al. (2015). Methane oxidation following submarine permafrost degradation: Measurements from a central laptev sea shelf borehole. *Journal of Geophysical Research: Biogeosciences*, *120*, 965–978. https://doi.org/10.1002/2014JG002862

Overduin, P. P., Rachold, V., & Grigoriev, M. N. (2008). The state of subsea permafrost in the western laptev nearshore zone. In D. L. Kane & K. M. Hinkel (Eds.), *Institute of northern engineering* (Vol. *2*, pp. 1345–1350). Faribanks, Alaska: University of Alaska Fairbanks.

Ponomarev, V. (1940). On the history of the Kozhevnikov Bay in the Quaternary. *Soviet Geology*, *11*, 95–101.

Ponomarev, V. (1960). *Subterranean waters in a region with a thick stratum of permanently frozen rocks*. Moscow: AN SSSR.

Portnov, A. D., Vadakkepuliyambatta, S., Mienert, J., & Hubbard, A. L. (2016). Ice-sheet-driven methane storage and release in the Arctic. *Nature Communications*, *7*, 10314.

Rachold, V., Bolshiyanov, D. Y., Grigoriev, M. N., Hubberten, H. W., Junker, R., Kunitsky, V. V., et al. (2007). Nearshore Arctic subsea permafrost in transition. *Eos, Transactions American Geophysical Union*, *88*(13), 149–150. https://doi.org/10.1029/2007EO130001

Razumov, S. O., Spektor, V. B., & Grigoriev, M. N. (2014). A Model of the Late Cenozoic cryolithozone evolution for the Western Laptev Sea shelf. *Okeanologiya*, *54*(5), 679–693.

Reimnitz, E., Barnes, P. W., Rearic, D. M., Minkler, P. W., Kempema, E. W., & Reiss, T. E. (1982). Marine geological investigations in the Beaufort Sea in 1981 and preliminary interpretations for regions from the Canning River to the Canadian Border. *U.S. Geological Survey Open-File Report*, *46*(974), 191–202. https://doi.org/10.3133/ofr82974

Rekant, P., Bauch, H. A., Schwenk, T., Portnov, A. D., Gusev, E., Spiess, R., et al. (2015). Evolution of subsea permafrost landscapes in Arctic Siberia since the Late Pleistocene: A synoptic insight from acoustic data of the Laptev Sea. *Arktos The Journal of Arctic Geosciences*, *1*(1), 11. https://doi.org/10.1007/s41063-015-0011-y

Rekant, P., & Vasiliev, A. (2011). Distribution of subsea permafrost at the Kara Sea shelf. *Cryosphere of the Earth*, *XV*, 69–72.

Romanovskii, N. N., Hubberten, H. W., Gavrilov, A. V., Tumskoy, V. E., & Kholodov, A. L. (2004). Permafrost of the east Siberian Arctic shelf and coastal lowlands. *Quarternary Science Reviews*, *23*, 1359–1369. https://doi.org/10.1016/j.quascirev.2003.12.014

Ruppel, C. D. (2015). Permafrost-associated gas hydrate: Is it really approximately 1% of the global system? *Journal of Chemical & Engineering Data*, *60*, 429–436. https://doi.org/10.1021/je500770m

Ruppel, C. D., Herman, B. M., Brothers, L. L., & Hart, P. E. (2016). Subsea ice-bearing permafrost on the U.S. Beaufort Margin: 2. Borehole constraints. *Geochemistry, Geophysics, Geosystems*, *17*, 4333–4353. https://doi.org/10.1002/2016GC006582

Ruppel, C. D., & Kessler, J. D. (2017). The interaction of climate change and methane hydrates. *Reviews of Geophysics*, *55*, 126–168. https://doi.org/10.1002/2016RG000534

Schirrmeister, L. (2007). *Expeditions in Siberia in 2005*, vol. 550. Bremerhaven, Germany: Alfred Wegener Institute for Polar and Marine Research. https://doi.org/10.2312/BzPM_0550_2007

Shakhova, N., & Semiletov, I. (2007). Methane release and coastal environment in the east siberian arctic shelf. *Journal of Marine Systems*, *66*, 227–243. https://doi.org/10.1016/j.jmarsys.2006.06.006

Sherman, D., Kannberg, P., & Constable, S. (2017). Surface towed electromagnetic system for mapping of subsea Arctic permafrost. *Earth and Planetary Science Letters*, *460*, 97–104. https://doi.org/10.1016/j.epsl.2016.12.002

Slagoda, E. A. (1993). Genesis i mikrostroenie kriolitogennykh otlozhenii Bykovskogo polyostrova i ostrova Muoastakh (genesis and microstructure of cryolithogenic deposits at the Bykovsky Peninsula and the Muostakh Island) (PhD thesis), Mel'nikov Permafrost Institute, Russian Academy of Sciences, Siberian Branch, Yakutsk.

Soloviev, V., Ginzburg, G., Telepnev, E., & Mikhaluk, Y. (1987). *Cryothermia and gas hydrates in the Arctic Ocean*. Leningrad, Russia: Sevmorgelogia.

Stevens, C. W., Moorman, B. J., & Solomon, S. M. (2010). Modeling ground thermal conditions and the limit of permafrost within the nearshore zone of the Mackenzie Delta, Canada. *Journal of Geophysical Research*, *115*, F04027. https://doi.org/10.1029/2010JF001786

Taylor, A. E., Dallimore, S. R., Hill, P. R., Issler, D. R., Blasco, S., & Wright, F. (2013). Numerical model of the geothermal regime on the Beaufort Shelf, arctic Canada since the Last Interglacial. *Journal of Geophysical Research: Earth Surface*, *118*, 2365–2379. https://doi.org/10.1002/2013JF002859

Tipenko, G. S., Romanovskii, N. N., & Kholodov, A. L. (1999). Simulation of the offshore permafrost and gas hydrate stability zone; Mathematical solution, numerical realization and records of test calculation. *Earth Cryosphere*, *III*, 71–78.

van Everdingen, R. O. (1998). *Multi-language glossary of permafrost and related ground-ice terms*. Calgary, Canada: International Permafrost Association, The University of Calgary Printing Services.

Vasiliev, A. A., Rekant, P. V., Oblogov, G. E., & Korostelev, Y. V. (2018). New GIS-oriented map of submarine Permafrost of the Kara Sea, *Reports of the Extended Session of the Scientific Council on Earth Cryology of the Russian Academy of Sciences: Current Problems of Geocryology* (Vol. 1, pp. 291–295). Moscow: KDU University Press.

Vigdorchik, M. E. (1980a). *Arctic Pleistocene history and the development of submarine permafrost*. Boulder, CO: Westview Press.

Vigdorchik, M. E. (1980b). *Submarine permafrost on the Alaskan continental shelf*. Boulder, CO: Westview Press.

Viscosi-Shirley, C., Pisias, N., & Mammone, K. (2003). Sediment source strength, transport pathways and accumulation patterns of the Siberian-Arctic's Chukchi and Laptev shelves. *Continental Shelf Research*, *23*, 1201–1225. https://doi.org/10.1016/S0278-4343(03)00090-6

Westermann, S., Schuler, T. V., Gisnås, K., & Etzelmüller, B. (2013). Transient thermal modeling of permafrost conditions in Southern Norway. *The Cryosphere*, *7*, 719–739. https://doi.org/10.5194/tc-7-719-2013

Whittaker, J., Goncharov, A., Williams, S., Müller, R. M., & Leitchenkov, G. (2013). Global sediment thickness dataset updated for the Australian-Antarctic Southern Ocean. *Geochemistry, Geophysics, Geosystems*, *14*, 3297–3305. https://doi.org/10.1002/ggge.20181

Winterfeld, M., Schirrmeister, L., Gerigoriev, M. N., Kunitsky, V. V., Andreev, A., Murray, A., & Overduin, P. P. (2011). Coastal permafrost landscape development since the Late Pleistocene in the western Laptev Sea, Siberia. *Boreas*, *40*(4), 697–713. https://doi.org/10.1111/j.1502-3885.2011.00203.x

Woodgate, R. A. (2018). Increases in the Pacific inflow to the Arctic from 1990 to 2015, and insights into seasonal trends and driving mechanisms from year-round Bering Strait mooring data. *Progress in Oceanography*, *160*, 124–154. https://doi.org/0.1016/j.pocean.2017.12.007

Zhigarev, L. (1997). *Submarine Cryolithozone (Okeanicheskaya Kriolitozona)*. Moscow: MSU Publishing.